A computational study of the interplay between viscoplasticity and hardening for impact-loaded uniform density foams

Bhanu Pratap Sharma[1, *] Amuthan A. Ramabathiran[2,†] Abhijit Gogulapati[1,‡]

[1] Department of Aerospace Engineering, Indian Institute of Technology Bombay, Mumbai, Maharahstra 400076, India.
[2] Aerospace Engineering, California Polytechnic State University, San Luis Obispo, CA 93407, USA.

Abstract

Foam-like materials have been studied extensively for applications requiring energy absorption and blast mitigation. This work analyzes the interplay between viscoplasticity—quantified by the rate-dependence and viscosity parameters—and various hardening rules for uniform density foams when they are subject to blast-like impact loads. The foam is modeled using a simple viscoplastic extension of the rate-independent elastoplastic model developed by Deshpande and Fleck and a flexible hardening rule that exhibits different qualitative hardening regimes. The constitutive model is implemented as a VUMAT in ABAQUS. The underlying elastoplastic wave mechanics under these different scenarios is also examined. The results presented here indicate a qualitative change in the foam response depending on the amount of viscoplasticity and the type of hardening behavior. Additionally, this study attempts to answer whether or not rate-dependency is always beneficial for mitigation of applied loads. The results presented in this work has important implications for the design of impact-resistant foams.

1 Introduction

The mechanical properties of foams render them valuable for applications requiring energy absorption under high-speed loading events. The current study caters to the specific application of mitigating blast waves using uniform-density foams (UDFs). In particular, we study the interplay between viscoplastic effects and hardening response in UDFs.

Numerous studies have analyzed UDFs from the viewpoint of blast mitigation, see Refs. [4, 6, 8, 9, 12–14, 18, 24]. Researchers have used experimental approach [4, 6, 8, 13, 14, 18], computational methods [4, 8, 9, 12, 13, 24], or analytical concepts from 1D shock theory [8, 9, 12, 13]. The typical analysis of foams for blast mitigation involves applying load at one end and recording either the end wall displacement or the transmitted force/pressure at the opposite end. In the former type of analysis, the end wall is a free surface as in Ref. [6] and in the latter type, it is a rigid wall as in Refs. [4, 8, 9, 12–14, 18, 24].

The applied load is typically chosen as one of the following: impacting a foam on a rigid surface, or by driving a rigid plate or mass to impact a stationary foam [9, 13], or using an actual blast

*bhanups1991@iitb.ac.in
†aramabat@calpoly.edu
‡agogulapati@iitb.ac.in

wave or a pressure pulse [4, 6, 8, 9, 12, 14, 18, 24]. The geometry of the foam is modeled either as a continuum [4, 8, 9, 13], or as a chain of 1D spring mass system [12], or as 2D/3D Voronoi cells.

To characterize the performance of the foams, a variety of metrics have been used by researchers, such as deceleration of the impactor/attenuation of impactor velocity [9], normalized or actual values of the peak crushing force, transmitted force, transmitted impulse [4, 6, 8, 9, 12–14, 18, 24], and back face deflection [6]. The performance of foams under high-speed loadings has been observed to depend on several parameters such as foam thickness [25], applied load [14], rate of loading or impact velocity [16], foam strength [13, 14], and densification strain [14, 25].

There is a substantial amount of literature on blast mitigation using foam–like materials of uniform density. However, to the best of our knowledge, not much work has been done to explore the effect of rate-dependency on the blast mitigation performance of foams. A possible explanation could be the focus on the analysis and characterization of available materials, which are nearly rate-independent. In this work, we devise constitutive models that exhibit a wide range of both viscoplastic and hardening behaviors, but we do not delve into the issue of whether actual foams with such properties exist.

The overall objective is to investigate the interplay of viscoplastic parameters and different types of hardening behaviors on the elastoplastic waves when a foam is subject to a sudden pressure pulse. The specific objectives are the following: (1) to study the effects of viscoplastic parameters on the foam's qualitative and quantitative response; (2) to understand qualitatively the effect of hardening on the viscoplastic response; and (3) to understand whether or not rate-dependent material behavior is a always beneficial for reducing peak pressures at the distal end. To meet these objectives, computational investigations are carried out using a uniform-density PU foam. All the simulations presented here are carried out using ABAQUS.

The organization of this paper is as follows. We introduce the constitutive model for viscoplastic UDFs in the next section, followed by a brief validation of the implementation of the model in ABAQUS. Supplementary information with details of the algorithmic implementation are provided in A. We then present exhaustive results for the propagation of elastoplastic waves in nearly one-dimensional bars and analyze the response. We conclude the paper with a discussion of the primary outcomes of this computational study, and in particular address the objectives raised above.

2 Materials and Methods

The constitutive model developed by Deshpande and Fleck [2] for crushable foam-like materials, hereafter referred to as the DF model, has been widely used in several numerical studies, like [5, 10], to study various aspects of the mechanical response of foams like plastic collapse at nearly constant stress and steep rise in stress after densification. The DF model has also been implemented in finite element software like ABAQUS. The DF model, however, is not directly applicable if the macroscopic mechanical behavior of the foam is rate-dependent. We propose in this work a simple viscoplastic extension of the DF model, hereafter referred to as the VP model, for foam-like materials. We augment the DF model on two fronts: (i) by adding a non-linear isotropic hardening law (see Eq. (6)), (ii) by using a viscoplastic flow rule developed by Perić [15] to model rate-dependency (see Eq. (9)). These simple modifications introduce two new material parameters, viscosity (μ) and rate parameter (η), and a mechanism to change the rate of densification upon plastic yielding. Thus, the extension of the DF model considered here is specifically tailored to study viscoplastic effects under varying levels of densification.

We present in this section the mathematical formulation of the VP model, followed by validation of the VP model in ABAQUS; details of the algorithmic implementation of the VP model are

provided in A.

2.1 Viscoplastic extension of DF model

We work within the small strain approximation regime, where an additive decomposition of the strain tensor of the form

$$\boldsymbol{\epsilon} = \boldsymbol{\epsilon}^e + \boldsymbol{\epsilon}^p, \tag{1}$$

is valid. The stress is related to the elastic strain as

$$\boldsymbol{\sigma} = \mathbf{D} : \boldsymbol{\epsilon}^{\mathbf{e}}. \tag{2}$$

To specify the evolution of the plastic strain $\boldsymbol{\epsilon}^p$, we first introduce the yield function ϕ as

$$\phi(\boldsymbol{\sigma}, \sigma_y) = \hat{\sigma} - \sigma_y = 0, \tag{3}$$

where,

$$\hat{\sigma} = \frac{1}{\sqrt{1 + \alpha^2/9}} \sqrt{\sigma_e^2 + \alpha^2 \sigma_m^2}, \tag{4}$$

is an equivalent von Mises stress. The elastic domain is related to the yield function as $\phi(\boldsymbol{\sigma}, \sigma_y) < 0$. The various terms in the equivalent von Mises stress (4) are defined as

$$\sigma_e = \sqrt{\frac{3}{2} \boldsymbol{s} : \boldsymbol{s}}, \tag{5a}$$

$$\sigma_m = \frac{1}{3} \mathrm{tr}(\boldsymbol{\sigma}), \tag{5b}$$

$$\alpha = \frac{3k}{\sqrt{9 - k^2}}, \tag{5c}$$

$$k = \sqrt{3(1 - 2\nu_p)}. \tag{5d}$$

Here, $\boldsymbol{s}$ is the deviatoric stress, σ_e and σ_m are the von Mises stress and the hydrostatic stress respectively, and ν_p is the plastic Poisson's ratio.

The first modification to the DF model that we propose is a new expression for the yield stress σ_y. We postulate the following dependence of the yield stress σ_y on the equivalent plastic strain $\hat{\epsilon}$, to be defined later (see Eq. (10)), as:

$$\sigma_y = A e^{\hat{\epsilon}(\hat{\epsilon} - D)C} + B\sqrt{\hat{\epsilon}} \ln(\hat{\epsilon} + P) \tag{6}$$

This specific form of the hardening response—controlled by five parameters A, B, C, D, and P—is chosen to simulate different rates of densification in the hardening response, as will be explained in a later section. Specifically, A is the initial yield stress, B controls the plateau region of the hardening curve, D is the densification strain, C controls the rate of densification, and P controls initial softening after the onset of yielding.

The second essential modification we make to the DF model is the introduction of viscoplastic effects. We chose a simple Perić type viscoplastic model [15] with an associative flow rule of the form

$$\dot{\boldsymbol{\epsilon}}^p = \dot{\gamma} \hat{\boldsymbol{n}} = \dot{\gamma} \frac{\boldsymbol{n}}{\|\boldsymbol{n}\|}, \tag{7}$$

where,

$$\boldsymbol{n} = \frac{\partial \phi}{\partial \boldsymbol{\sigma}} = \left(\frac{1}{1 + \alpha^2/9} \right) \frac{1}{\hat{\sigma}} \left[\frac{3}{2} \boldsymbol{s} + \frac{\alpha^2}{3} \sigma_m \boldsymbol{I} \right], \tag{8}$$

and,

$$\dot{\gamma} = \begin{cases} \frac{1}{\mu}\left[\left(\frac{\hat{\sigma}}{\sigma_y}\right)^{\frac{1}{\eta}} - 1\right], & \text{if} \quad \phi(\boldsymbol{\sigma}, \sigma_y) \geq 0, \\ 0, & \text{if} \quad \phi(\boldsymbol{\sigma}, \sigma_y) < 0. \end{cases} \tag{9}$$

The constants μ and η represent the viscosity and the rate-dependency parameters, respectively, and serve as the primary means by which we alter the viscoplastic response in this work. We note for the sake of completeness that the rate-independent model is recovered in the limit $\mu \to 0$, $\eta \to 0$.

To complete the specification of the VP model, we define the equivalent plastic strain $\hat{\epsilon}$ via the relation

$$\dot{\hat{\epsilon}} = \dot{\gamma}. \tag{10}$$

In the special case when $\|\boldsymbol{n}\| = 1$, the equivalent plastic strain defined above satisfies the work conjugacy relation

$$\boldsymbol{\sigma} : \dot{\boldsymbol{\epsilon}}^p = \hat{\sigma}\dot{\hat{\epsilon}}. \tag{11}$$

The condition $\|\boldsymbol{n}\| = 1$ is satisfied when the plastic Poisson's ratio is negligible: $\nu_p \to 0$. For collapsible materials $\nu_p \to 0$ has been observed experimentally—see [3, 17, 22, 26].

In summary, the VP model proposed here requires the specification of 10 material parameters: two for isotropic elasticity matrix $\mathbf{D}$ (elastic modulus, E, and elastic Poisson's ratio, ν), five for defining the shape of the hardening curve (A, B, C, D, P), one for the shape of the yield surface (plastic Poisson's ratio, ν_p), and two for the viscoplastic flow rule (viscosity, μ, and rate-dependence, η). In the current study, the initial yield stress (A), the elastic constants (E and ν) and the plastic Poisson's ratio (ν_p) are fixed—the values of these parameters are taken from Refs. [11, 17] for a rigid polyurethane foam of density 204 kg/m^3. The rest of the parameters are chosen so as to obtain different types of hardening behavior (see Table 1). The three sets of parameters shown in Table 1 differ in values of hardening parameters C and D which, as noted earlier, control the rate of densification and the width of the plateau region, respectively. Specifically, *Case 1* and *Case 3* capture two extreme cases: *Case 1* corresponds to a long plateau region combined with an almost linear hardening behavior, while *Case 3* corresponds to a short plateau followed by a steep hardening behavior, i.e., a high rate of densification (see Figure 1). *Case 2* provides an intermediate hardening behavior that is roughly halfway between these *Case 1* and *Case 3*. These three sets of parameters are thus chosen to model foams with different types of hardening behavior.

2.2 Verification of the constitutive model implementation

We implement the viscoplastic constitutive equations (1) to (9) using the standard return mapping algorithm with an elastic predictor followed by viscoplastic correction under the general framework of small-strain plasticity [19, 20]. A vectorized user material subroutine (VUMAT) is used to implement the described model in the explicit finite element solver of ABAQUS. Details of the algorithmic implementation are presented in A. We present here a few results that validate our numerical algorithm.

FE simulations were performed in ABAQUS with the following setting. A mesh consisting of a total of 27 finite elements is used for these tests. The 8 noded solid element is used with reduced order integration (element type C3D8R). Since the purpose is to simply verify the correctness of implementation, therefore, arbitrary non-zero values are assigned to the material parameters $(\mu, \eta, A, B, C, D, P)$, see Table 1.

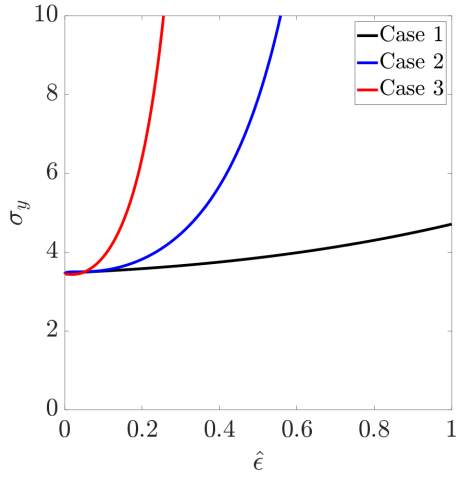

Figure 1: Evolution of the yield stress (σ_y) with equivalent plastic strain ($\hat{\epsilon}$) for the three hardening cases (see Equation (6)).

2.2.1 Consistency with DF model in the limit $\mu, \eta \to 0$

In the limiting case where $\mu \to 0$ (no viscosity) and $\eta \to 0$ (no rate dependence), the VP model reduces to DF model, which has a native implementation in ABAQUS. We validate our algorithmic implementation of the VP model by comparing it with the predictions of the DF model in this limit. These results are shown in Figures 2 and 3.

Alternatively, the response of the VP model and the DF model converge even for non-zero values of viscosity (μ) and rate-dependency (η) if the applied strain-rate keeps decreasing as shown in Figure 6.

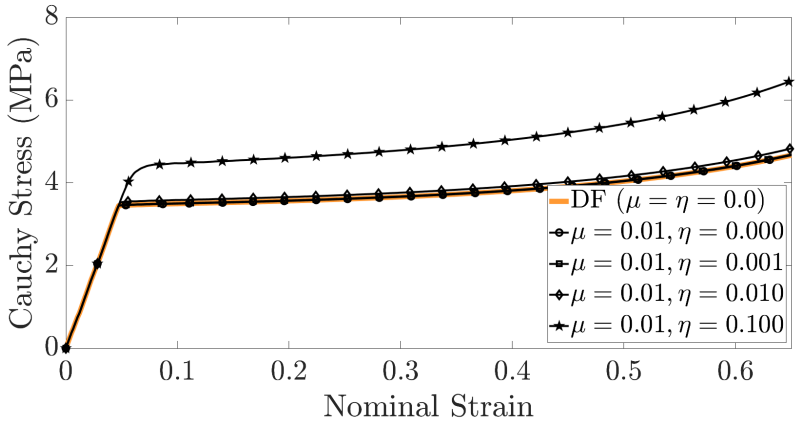

Figure 2: Stress versus strain response showing convergence of VP model to DF model as μ and η approach 0. Simulations done for a fixed value of $\mu = 0.01$ and $\dot{\epsilon} = 1000$.

2.2.2 Creep, stress relaxation, and strain rate response

Additionally, the following standard checks of viscoplasticity were performed to verify the correctness of the numerical implementation of the VUMAT: (1) a creep test where the strain versus time

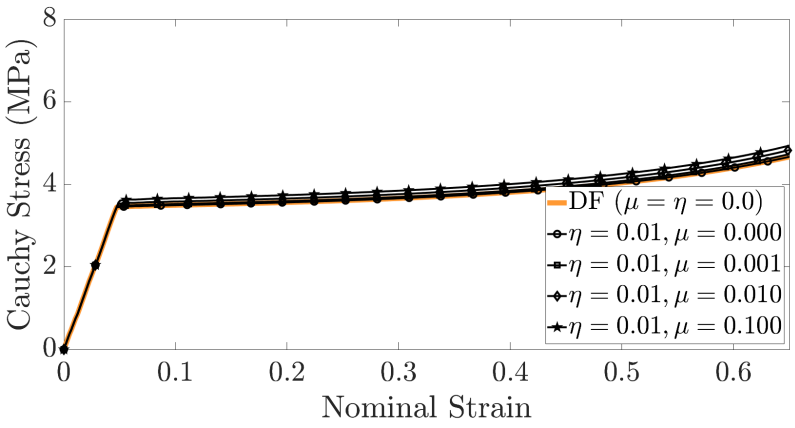

Figure 3: Stress versus strain response showing convergence of VP model to DF model as μ and η approach 0. Simulations done for a fixed value of $\eta = 0.01$ and $\dot{\epsilon} = 1000$.

response is observed under constant applied stress; (2) a stress-relaxation test, where the stress versus time response is observed under constant applied strain; and (3) a strain-rate dependence test where stress versus strain response is observed under different values of applied strain rates.

The results of FE simulations for the creep, stress relaxation, and strain rate dependence tests are shown in Figures 4, 5, and 6, respectively. Note that, the material is in the state of compression, and the plots show the absolute values of stresses and strains. From these results, it is evident that the VP model captures various aspects of viscoplastic behavior. In summary, these observations show that the computational implementation of the VP model is correct.

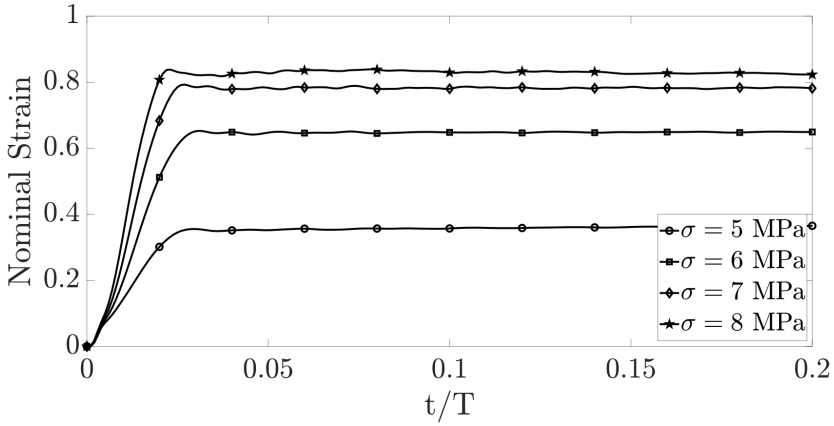

Figure 4: Creep test: Evolution of strain versus time for different values of applied stress.

3 Results and Discussion

We now turn to the primary topic of investigation of this work, namely the interplay between hardening and viscoplastic response. We present numerical simulations of shock tube experiments, as shown in Figure 7a. A block of uniform-density foam of length 25mm and square cross-section of 3mm $\times$ 3mm is subjected to a nearly rectangular pressure pulse as shown in Figure 7b. In this

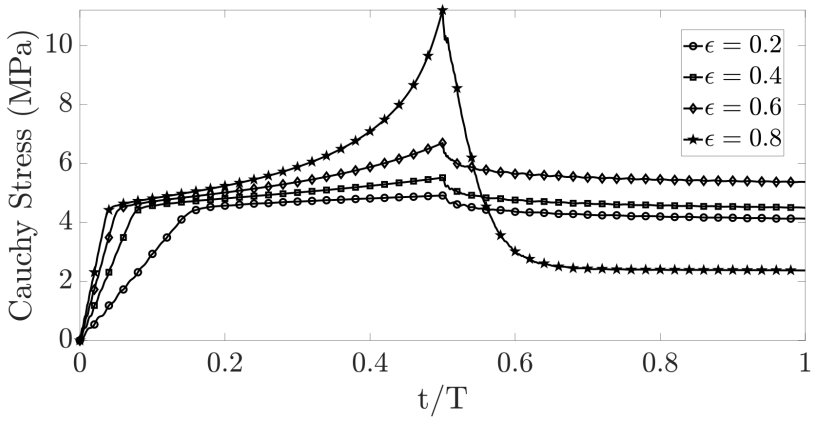

Figure 5: Stress relaxation test: Evolution of stress versus time for different values of applied strain, with strain rate $\dot{\epsilon} = 500s^{-1}$.

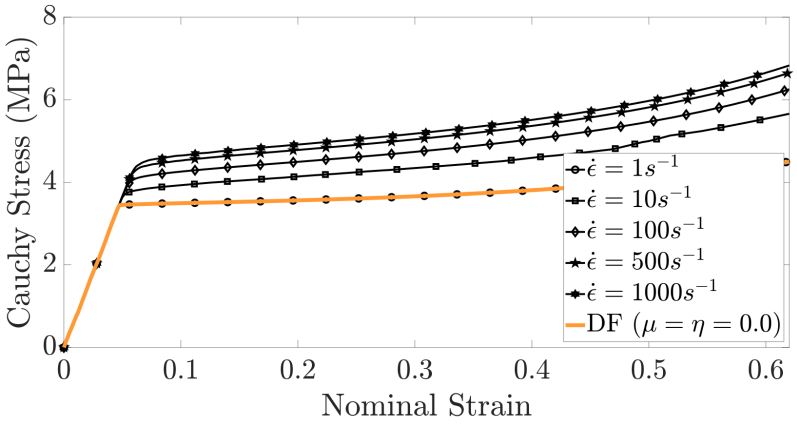

Figure 6: Strain rate dependence test: Stress versus strain response for different rates of applied strain.

study, a fixed peak pressure (P_{max}) equal to twice the initial yield stress (given by the material parameter A) is applied at one end of the foam. The load is applied for a pulse duration of $t_p = 0.1$ ms. The rise and decay time of the pulse are set to a small value ($\sim t_p/50$) compared to the pulse duration. The objective is to simulate the response of the foam sample subject to rapid impulsive loads like blast waves. Note that the following assumption is central to these simulations: the phenomenological viscoplastic description of the foam remains unchanged at elevated strain rates. The pressure pulse impacts the stationary foam that rests against a rigid wall. The side where the wave impinges is called the *proximal* end ($x = 0$) and the opposite end is called the *distal* end ($x = l$). The equivalent boundary value problem used in the FE simulations is shown in Figure 7c. Eight noded 3D elements with reduced integration (C3D8R) are used. Spatial and temporal sensitivity analyses are used to finalize the mesh size and integration time-step respectively as 1mm and 1E-8s. The FE model has 225 elements arranged in 25 layers with each layer containing 9 elements (3 along each direction). Symmetric boundary conditions (YSYMM and ZSYMM in ABAQUS terminology) are imposed on the lateral surfaces. These result in a restriction on the out-of-plane translation and rotation degrees of freedom of the nodes on the lateral surfaces. These

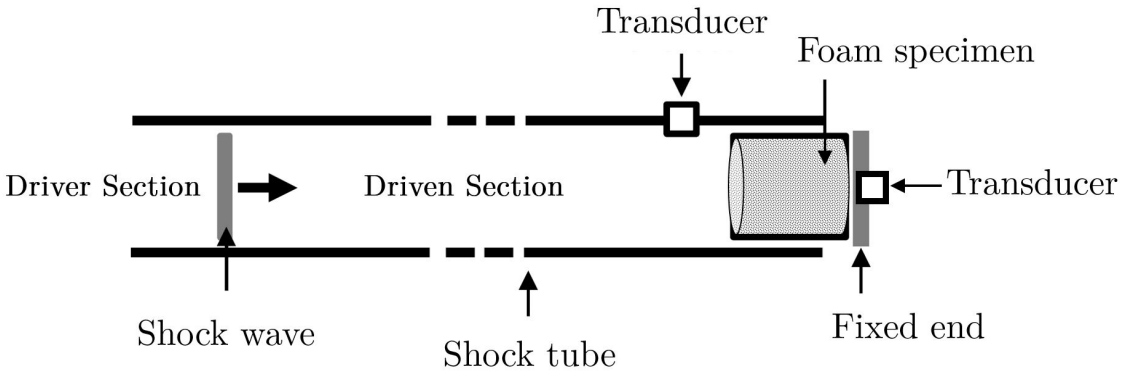

(a) Schematic of shock tube

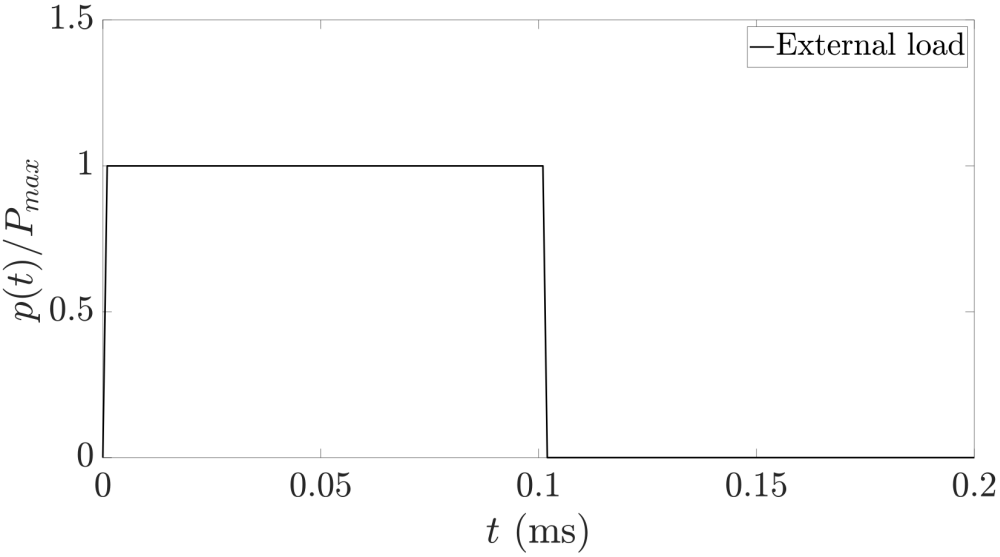

(b) Schematic of shock pulse

(c) Schematic of BVP modeled

Figure 7: A typical shock-tube experiment, the shock pulse, and equivalent BVP for FE analysis.

are described in Equations (12a) to (12c), valid for all time instants $t \in \mathbb{R}^+$

$$u_x(l,t) = 0, \tag{12a}$$

$$u_y = \theta_x = \theta_z = 0, \quad \forall \quad \boldsymbol{x} \in \partial B_y, \tag{12b}$$

$$u_z = \theta_x = \theta_y = 0, \quad \forall \quad \boldsymbol{x} \in \partial B_z, \tag{12c}$$

$$\boldsymbol{F}(0,t) = p(t)\boldsymbol{A}. \tag{12d}$$

where, u_x, u_y, u_z, are the displacements along the three spatial directions; ∂B_y and ∂B_z are the boundary surfaces with normal vectors along y and z directions; and $p(t)$ is the pressure acting along x on the proximal end of the prismatic block of foam with cross-section area $\boldsymbol{A}$.

In the simulations presented in this study, the response of the foam is characterized by a non-dimensional quantity $\tilde{p}$ defined as

$$\tilde{p} = \max\left(\frac{\sigma_{xx}(l,t)}{P_{max}}\right). \tag{13}$$

$\tilde{p}$ is the ratio of the peak value of the transmitted longitudinal stress at the distal end of the foam to the peak stress applied at the proximal end. Thus $\tilde{p} > 1$ and $\tilde{p} < 1$ corresponding to an amplification and mitigation of the blast wave, respectively. The metric $\tilde{p}$ is computed for different combinations of viscosity (μ) and rate-dependence (η) for the three cases of hardening presented earlier. To facilitate the parametric study, both μ and η are normalized using their minimum and maximum values according to Equation (14).

$$\begin{aligned} \bar{\mu} &= \frac{\mu - \mu_{min}}{\mu_{max} - \mu_{min}} \\ \bar{\eta} &= \frac{\eta - \eta_{min}}{\eta_{max} - \eta_{min}} \end{aligned} \tag{14}$$

Additionally, xt-plots are also presented to illustrate the elastic and plastic waves that are initiated due to the impact loads, and to explain the observed trends. The values of the material parameters used to generate the trend plots are shown in Table 1.

Table 1: Values of the parameters used for verification of the VP model and in the simulations for three different hardening behaviors.

Parameter	Verification	Case 1	Case 2	Case 3
E	71.4	71.4	71.4	71.4
ν	0.18	0.18	0.18	0.18
ν_p	0.0	0.0	0.0	0.0
μ	0.3	[0.01,1.0]	[0.01,1.0]	[0.01,1.0]
η	0.04	[0.01,1.0]	[0.01,1.0]	[0.01,1.0]
A	3.5	3.44	3.44	3.44
B	1.5	0.511	0.511	0.511
C	0.3	0.232	5.0	20.0
D	0.6	0.1	0.2	0.05
P	2.0	1.5	5.0	1.5

3.1 Effect of viscoplasticity for different hardening rules

Figure 8a shows the variation of $\tilde{p}$ for different combinations of viscosity and rate-dependence values for Case 1. It is observed that mitigation (if present) is observed only for lower values of viscosity (μ) and rate-dependence (η). In other words, mitigation performance deteriorates with increasing μ and η. Furthermore, mitigation performance is more sensitive to the changes in rate-dependence (η) as compared to those in viscosity (μ). Moreover, as per the metric of interest ($\tilde{p}$) there is no mitigation of the peak applied pressure for the second and third set of parameters, namely Case 2 and 3 (see Figure 8c for color plot and Figure 9, 10 for exact values). Note that the material exhibits a high densification rate or steep hardening curve for Case 2 and 3 parameters.

The data presented in Figure 8 is also shown separately using line plots for clarity in Figure 9 and 10. For Case 1, the lowest $\tilde{p}$ values are observed when the material approaches the rate-independent case ($\eta \to 0$). Unlike Case 1, the lowest $\tilde{p}$ value are observed for a non-zero values of η for both Case 2 and 3 indicating that a viscoplastic material behavior might result in a lower amplification of the peak pressure than the rate-independent material. The exact mechanics behind the final $\tilde{p}$ values is discussed in the following section.

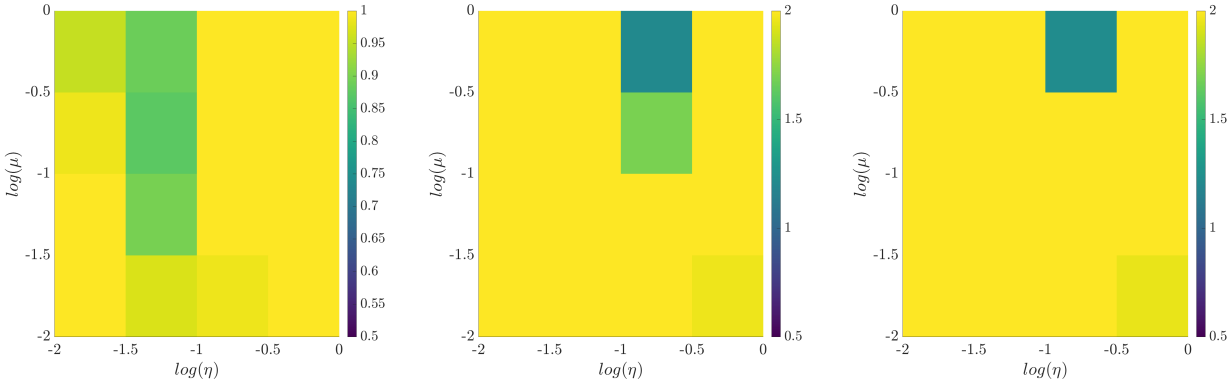

(a) Case 1 (b) Case 2 (c) Case 3

Figure 8: Effect of viscosity and rate-dependence on the metric of interest for the three different types of hardening behaviors.

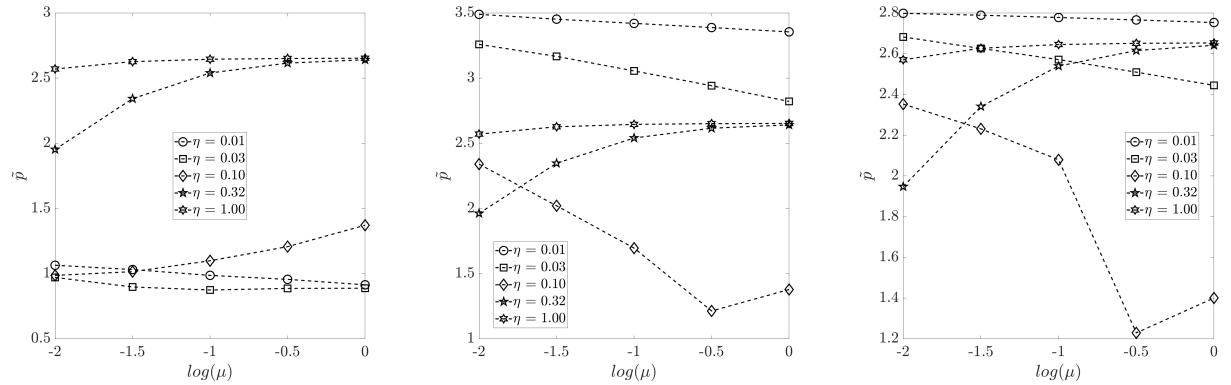

(a) Case 1: $\tilde{p}(\mu)$ (b) Case 2: $\tilde{p}(\mu)$ (c) Case 3: $\tilde{p}(\mu)$

Figure 9: Effect of viscosity on metric of interest for different levels of rate-dependence (vertical slices taken from Figures 8a, 8b, and 8c).

3.2 Mechanics of elasto-plastic waves inside the foam

The mechanics of elasto-plastic waves are conveniently studied using xt plots of the stress field. A vertical slice from an xt-plot shows the stress history at a specific location over time, while a horizontal slice shows the stress distribution over the length of the bar at a particular time instant. In particular, the vertical slice at $x/l = 1$ represents the stress history at the distal end. The peaks in the distal end stress appear as bright colors along the right edge of the xt-plot, with the brightest

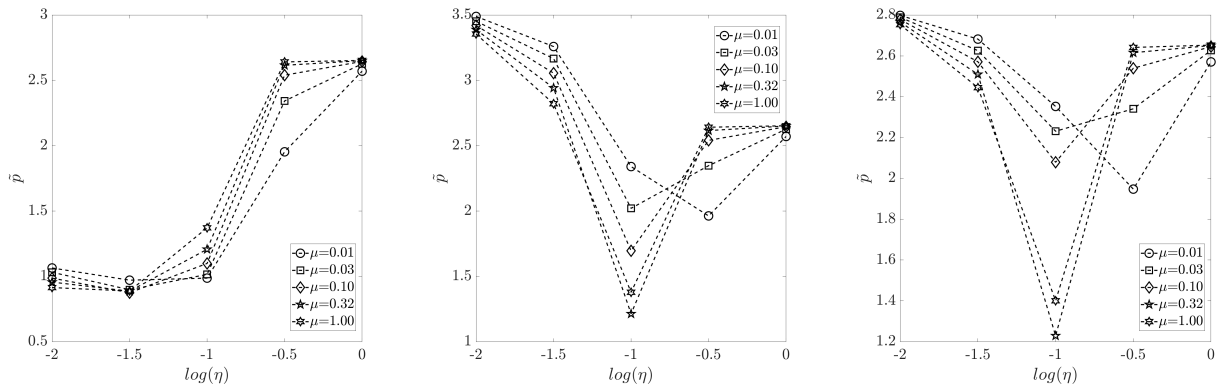

(a) Case 1: $\tilde{p}(\eta)$ (b) Case 2: $\tilde{p}(\eta)$ (c) Case 3: $\tilde{p}(\eta)$

Figure 10: Effect of rate-dependence on metric of interest for different levels of viscosity (horizontal slices taken from Figures 8a, 8b, and 8c).

color representing the metric of interest, $\tilde{p}$. The sensitivity of the wave motion to a given input parameter dictates the resulting changes in the xt-plots and consequently the metric of interest ($\tilde{p}$). Note that the color in the xt-plots for stress shows the local longitudinal stress divided by instantaneous local yield stress. The x-axis and y-axis of all the xt-plots shown in the current study are non-dimensionalized using respectively the characteristic length (or foam length or thickness, l) and time taken by the elastic wave to traverse the entire foam length once ($t_c = l/\sqrt{E/\rho}$).

The effect of increasing the viscoplastic parameters (viscosity and rate-dependence) on the elastoplastic waves for Case 1, Case 2, and Case 3 are respectively shown in Figures 12, 13, and 14. The xt-plots are arranged such that the plot on the bottom left corresponds to lowest values of μ and η with μ increasing vertically (bottom to top) and η increasing horizontally (left to right) (see Table 1 for μ, η range). Moreover, for comparison, the xt-plots obtained using the rate-independent DF model for all three cases are provided in Figure 11. These results clearly indicate a qualitative change in the elastoplastic wave propagation as the rate of densification increases. In particular, elastic unloading resulting in tensile waves are absent when the rate of densification is sufficiently high.

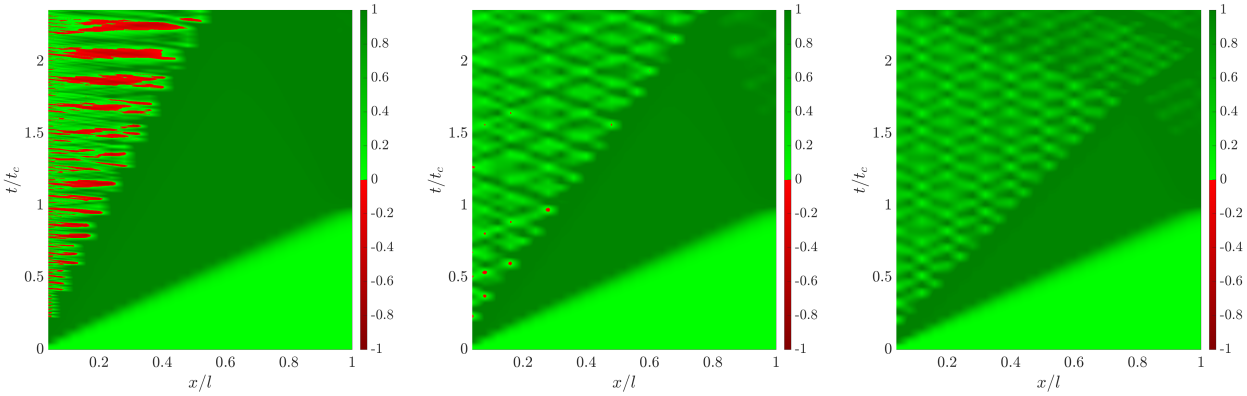

(a) Case 1 (b) Case 2 (c) Case 3

Figure 11: Elastoplastic stress waves obtained using the rate-independent DF model ($\mu = \eta = 0$). The stress is normalized by the local instantaneous yield stress.

We now turn to the elastoplastic response for UDFs with the VP model for their constitutive law. For low values of $\bar{\eta} = 0$, two distinct waves originate from the proximal end ($x = 0$) i.e., elastic precursor wave and a wave of plastic collapse or compaction wave. As the value of $\bar{\eta}$ increases, the effective yield stress of the material increases for the same rate of applied loading. Consequently, the possibility of the initiation of plastic collapse decreases. This is indicated by the transition in the qualitative nature of the xt-plots from left-most plot (for $\bar{\eta} = 0$) to the right-most plot (for $\bar{\eta} = 1.0$). This is also evident from the history of distal end stress shown in Figures 15. Specifically, for all values of $\bar{\mu}$, if $\bar{\eta} \leq 0.022$, the stress rises to its peak value in a smooth two step jump, first at $t/t_c = 1$ (elastic wave) and then at $t/t_c \sim 5$ (plastic wave).

On the contrary, for higher values of rate-dependence ($\bar{\eta} \geq 0.091$), the stress rises to the peak value in a single jump at $t/t_c = 1$ followed by high frequency oscillations. These oscillations are a result of the secondary compression and rarefaction waves bouncing back and forth between the distal end and the plastic wave generated as a result of the reflection of the elastic wave from the distal end. For high values of $\bar{\eta}$, the absence of a follower compaction wave from the proximal end implies that the initial yield stress of the material is higher than the applied peak pressure i.e., $\sigma_{yo} > P_{max}$.

Additionally, for all the values of $\bar{\eta}$ the elastic precursor wave's reflection from the distal end results in the formation of a local plastic region near the distal end, this implies that the following condition is met at the distal end: $\sigma_{x=l} > \sigma_{yo}$.

Consequently, the above two conditions result in a higher distal end stress than the external peak-pressure i.e., $\sigma_{x=l} > P_{max}$. This is also evident from the gradual increase in the amplitude of the first peak in Figure 15 and 16. The first peak is a result of the reflection of the elastic precursor wave from the distal end at $t/t_c = 1$. As $\bar{\eta}$ increases, the the value of $\tilde{p}$ rises, resulting in greater amplification of the applied load.

The above observations hold true irrespective of the shape of the hardening curve. This is evident by the similar trends observed when Case 3 parameters are used (see Figure 14 for xt-plots and Figures 19 for distal end stress histories). However, as a result of the change in the hardening parameters, there is a key difference in the slope of the follower plastic wave in the xt-plots and in the time at which the distal end stress attains its peak for low values of $\bar{\eta}$. Specifically, the speed of the plastic wave is highest for Case 3. The speed of the plastic wave is given by $v_p = \sqrt{E_t/\rho}$, where E_t is the instantaneous slope of the stress-strain curve after initial yield. Because of high rate of densification, E_t is comparatively much higher and thus the speed of the plastic wave is also higher. As a result, the plastic wave originated from the proximal end meets the plastic wave originated from the distal end wave much sooner than in Case 1. This results in the formation of a stronger compaction wave that travels toward the distal end resulting in a higher amplification of distal end stress (compare the amplitudes of the peaks in Figure 15b at $t/t_c \sim 5$ and in Figure 19b at $t/t_c \sim 2$).

Unlike the effect of the rate-dependence parameter, the qualitative nature of the elastoplastic waves remains relatively unchanged with changes in the viscosity. This is indicated by the qualitative similarity in the xt-plots positioned on the bottom edge ($\bar{\mu} = 0.0$) and the ones on the top edge ($\bar{\mu} = 1.0$). However, the exact amplitude of the distal end stress is affected by changes in viscosity (μ). This is evident from the amplitudes of the first two jumps in the distal end stress histories particularly for $\bar{\eta} = 0.091$ (see Figure 16, 18, and 20 respectively for Case 1, 2 and 3). Specifically, for a fixed level of rate-dependence, with increasing viscosity, the first jump (caused by the reflection of the elastic wave) grows in amplitude while the second jump (caused by the compaction wave hitting the distal end) falls in amplitude. Moreover, for $\bar{\eta} \leq 0.091$ the frequency of secondary wave reflections grows with increasing viscosity.

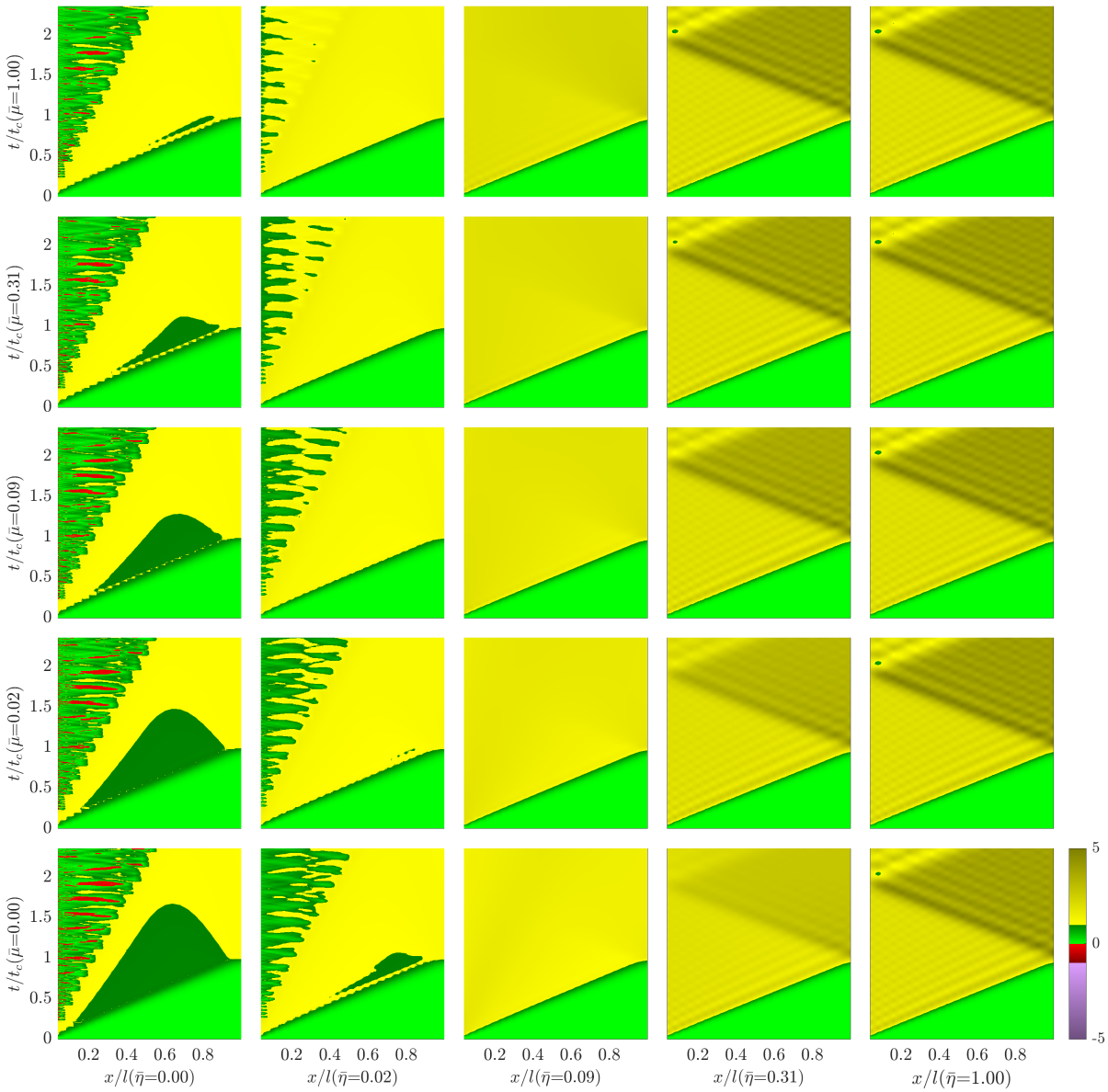

Figure 12: Effect of increasing the viscosity (μ) and rate-dependence (η) parameters on the elastoplastic waves for Case 1. Each xt-plot shows the non-dimensional longitudinal stress as a function of position and time for a fixed μ and η value.

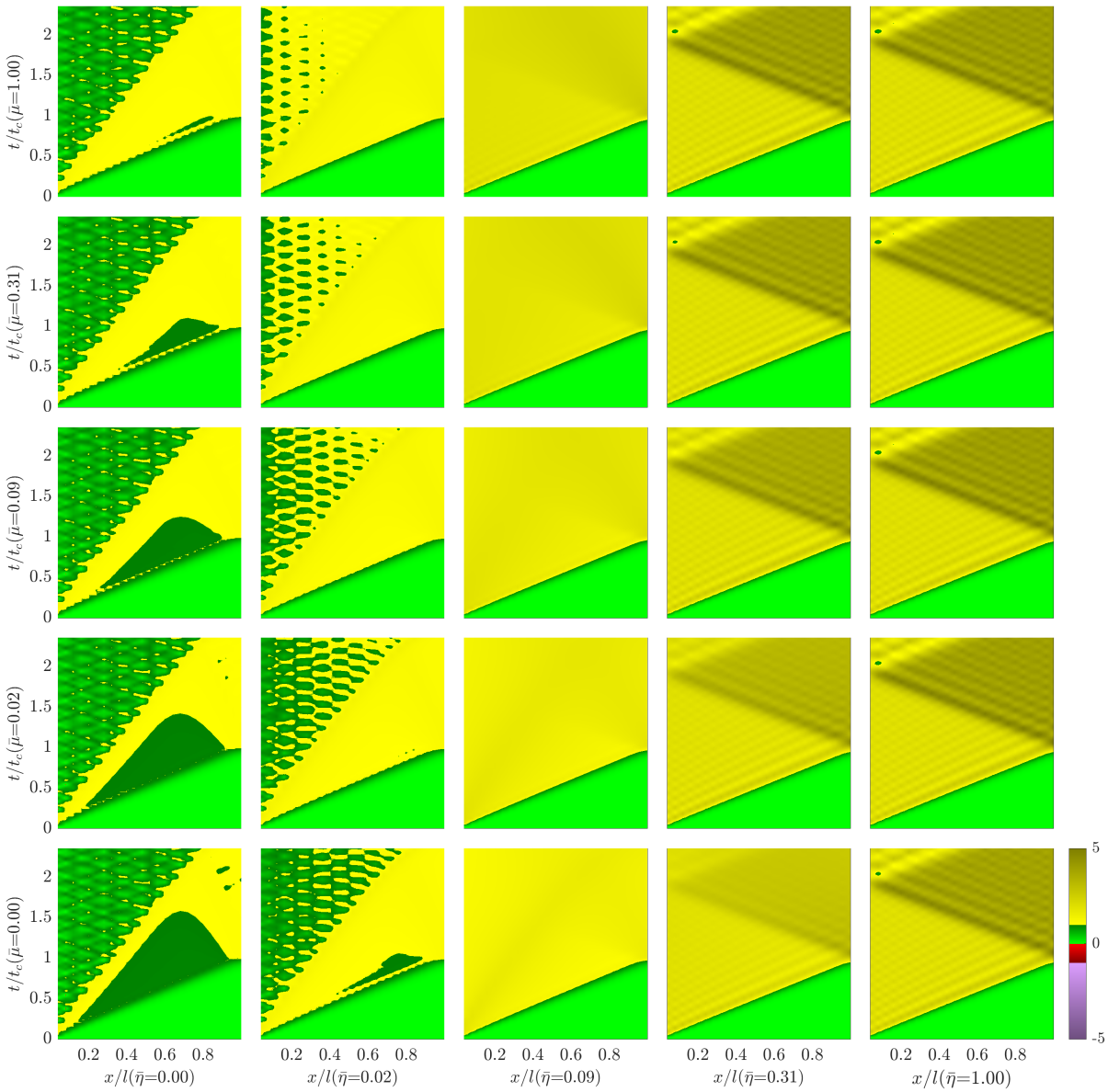

Figure 13: Effect of increasing the viscosity (μ) and rate-dependence (η) parameters on the elastoplastic waves for Case 2. Each xt-plot shows the non-dimensional longitudinal stress as a function of position and time for a fixed μ and η value.

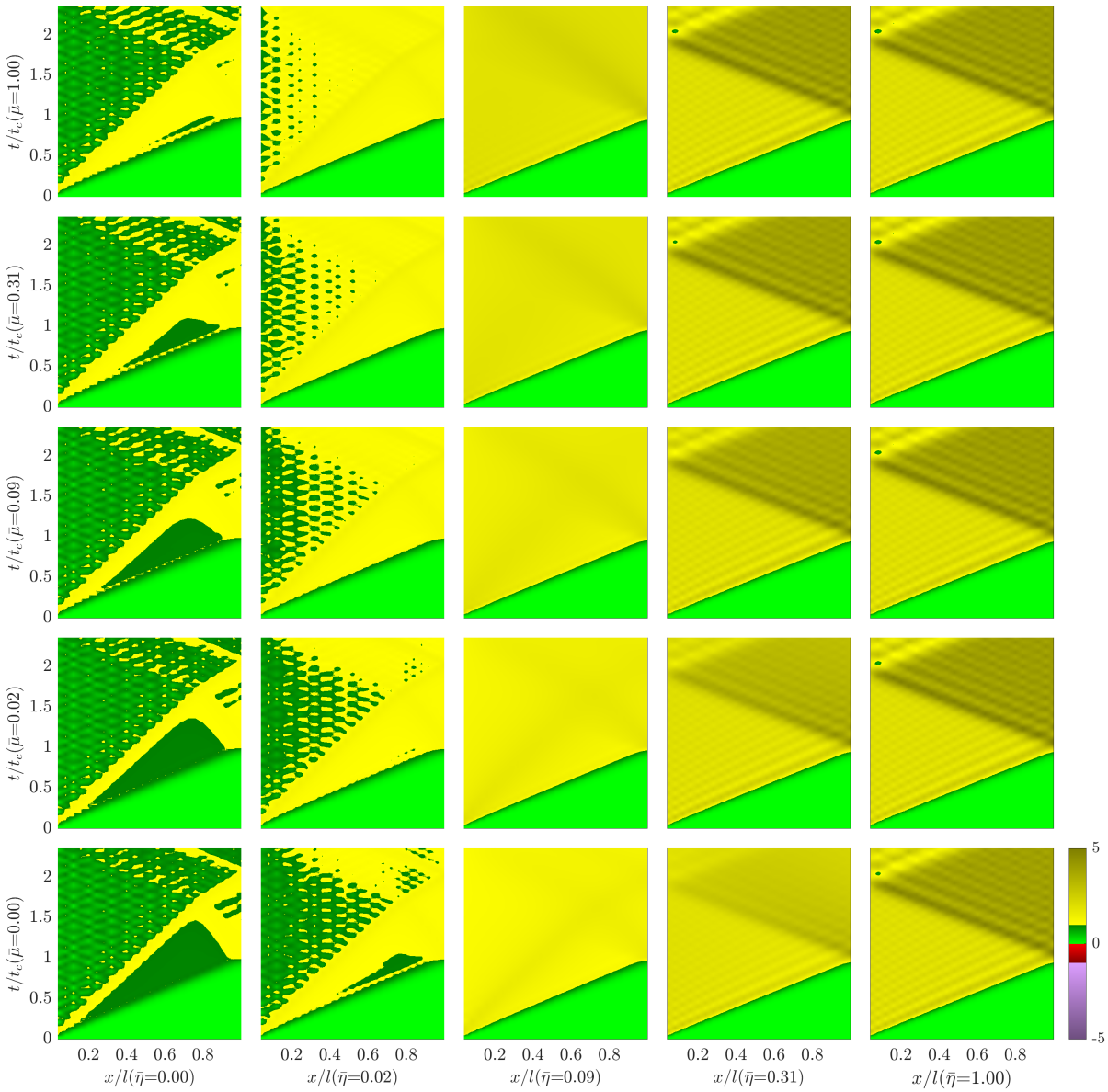

Figure 14: Effect of increasing the viscosity (μ) and rate-dependence (η) parameters on the elastoplastic waves for Case 3. Each xt-plot shows the non-dimensional longitudinal stress as a function of position and time for a fixed μ and η value.

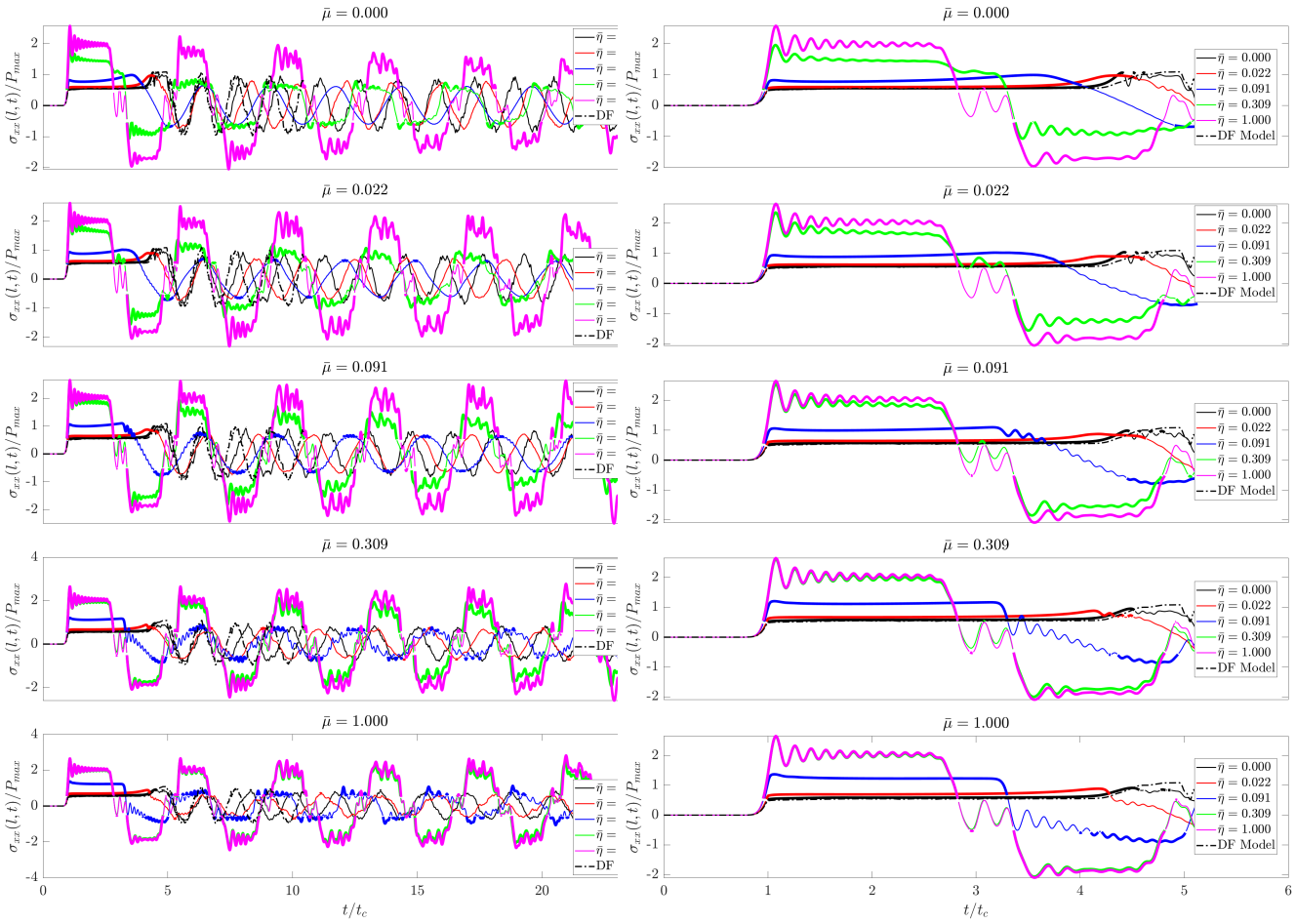

(a) (b)

Figure 15: History of the non-dimensional longitudinal stress at the distal end for Case 1 (Results grouped for $\bar{\eta}$ values): (a) response for the full duration; (b) zoomed the initial region.

4 Conclusions

This study presented the implementation, verification, and validation (parameter-fitting) of a simple viscoplastic extension of the DF model. The model was used to study the interplay between viscoplasticity and hardening in UDFs. Three different hardening laws with increasing rates of densification were considered. The key findings of the present study are summarized below:

1. Based on the metric used in the present study ($\tilde{p}$), low values (near zero) of viscosity and rate-dependence are suitable for mitigation if the material does not exhibit a steep hardening.

2. On the other hand, if the material shows a steep hardening behavior, a viscoplastic material behavior can result in a lower peak distal end stress. Note that this is still higher than the applied peak pressure and based on the metric used in the current study, it does not mitigate the applied load.

3. For a foam with short plateau region and steep hardening behavior, the speed of the plastic wave is higher and eventually results in a stronger distal end stress at an earlier time. On

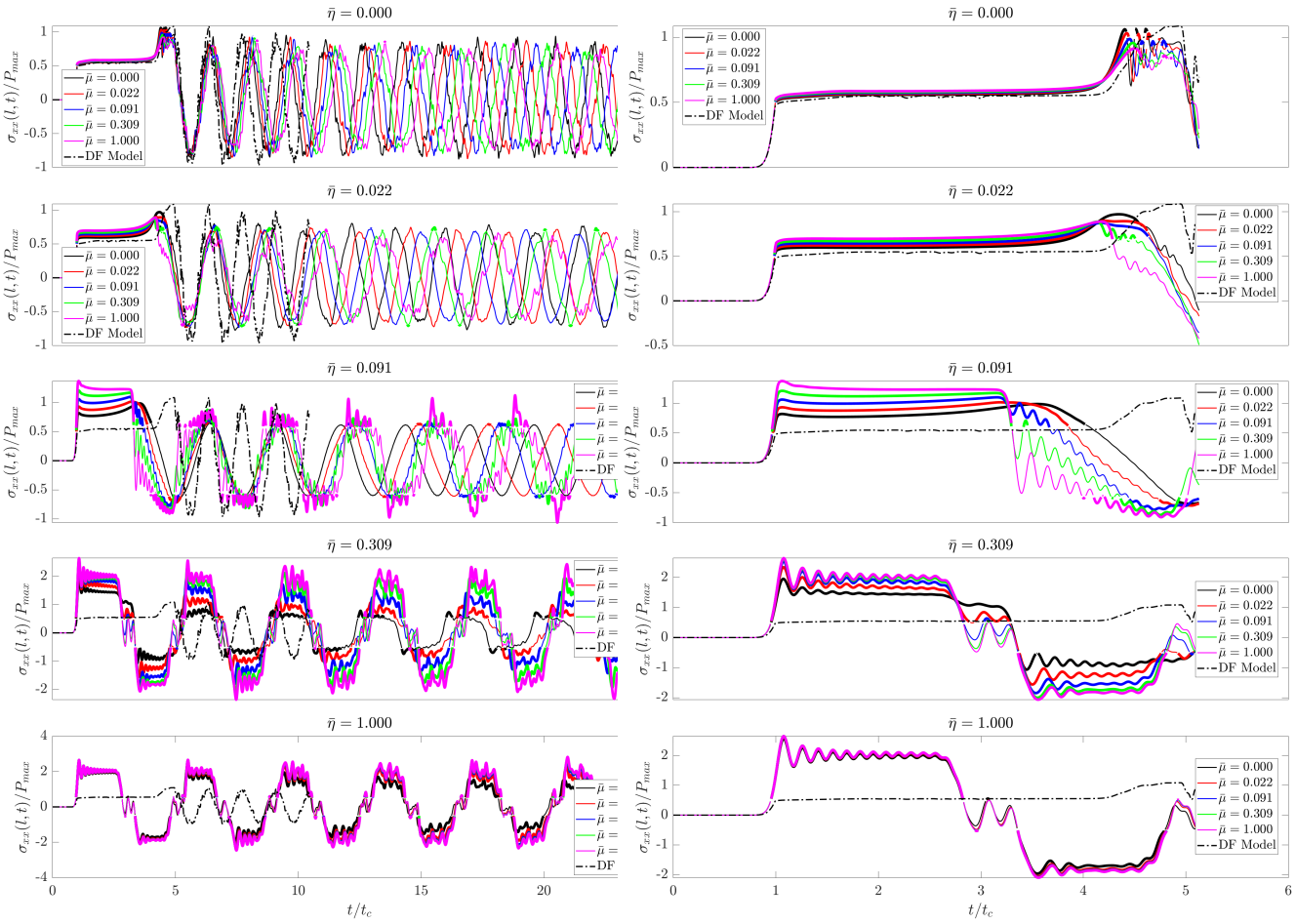

Figure 16: History of the non-dimensional longitudinal stress at the distal end for Case 1 (Results grouped for $\bar{\mu}$ values): (a) response for the full duration; (b) zoomed the initial region.

the contrary, the peak is delayed if the foam shows a relatively longer plateau and flatter hardening behavior.

4. In the framework of the VP model presented in this study, the foam's performance is more sensitive to changes in the rate-dependence parameter. Consequently, when η is increased, the benefits of viscoplastic regularization are readily negated by significant changes in both the qualitative and quantitative response of the foam. Moreover, if the rate-dependence parameter is too low or too high in magnitude, the foam's response is almost insensitive to changes in viscosity. The relative sensitivity with respect to viscosity is maximum for intermediate values of rate-dependence parameter. Therefore, to leverage the stability obtained from viscoplastic regularization, it is recommended to adjust the viscosity parameter and set the rate-dependence parameter to a near zero value to avoid deviations from the near-rate-independent behavior.

We wish to emphasize that the proposed model assumes homogeneous deformation under compression. We acknowledge that foams, both polymeric and metallic, are known to exhibit inhomogeneous deformation under quasi-static and low-velocity impact conditions [1, 23]. Macroscopically,

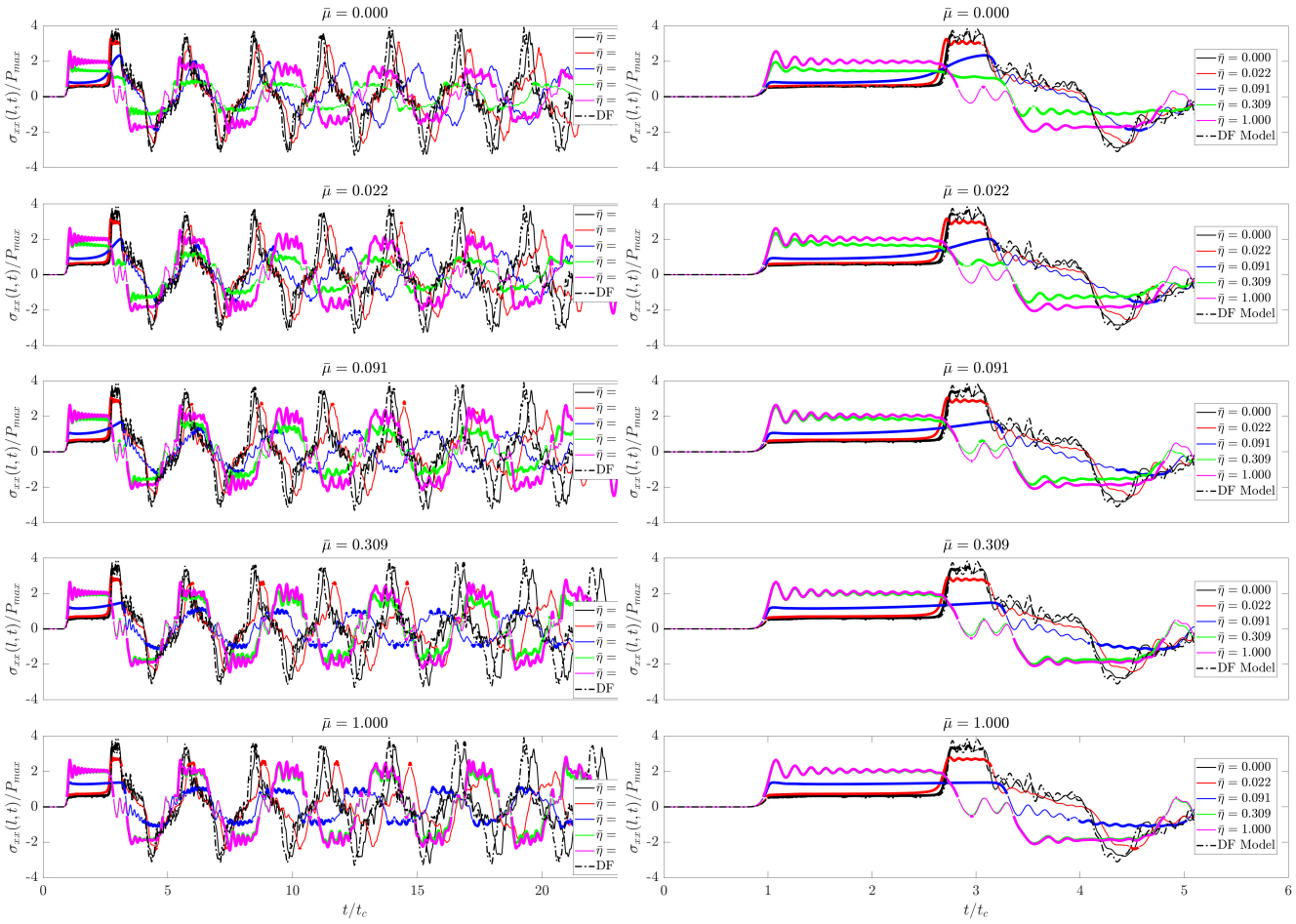

(a) (b)

Figure 17: History of the non-dimensional longitudinal stress at the distal end for Case 2 (Results grouped for $\bar{\eta}$ values): (a) response for the full duration; (b) zoomed the initial region.

these result in the formation of crush bands as a consequence of the inherent heterogeneity of the foam's geometry. These are reflected as undulations and sharp dips in the plateau region of the foam's stress-strain curve. Further, the material exhibits a softening behavior macroscopically as a result of the localized cell damage in the crush bands. The current model assumes a monotonic strain hardening in the plateau region and therefore assumes a homogeneous deformation. The rationale behind this assumption is the following: experimental and computational evidence from the literature [1, 7, 21] indicates that at high strain rates—relevant to the loading conditions simulated in this study—the foam response is characterized by two distinct regions separated by a propagating shock front, with both regions undergoing relatively homogeneous deformation. Accordingly, we have adopted the assumption of homogeneous deformation in this work. While we recognize that this is a simplifying assumption, it allows us to focus on the effect of different material parameters on the mechanics of elastoplastic shock waves generated in the foam. A detailed investigation of the consequences of this assumption will be pursued in a future work.

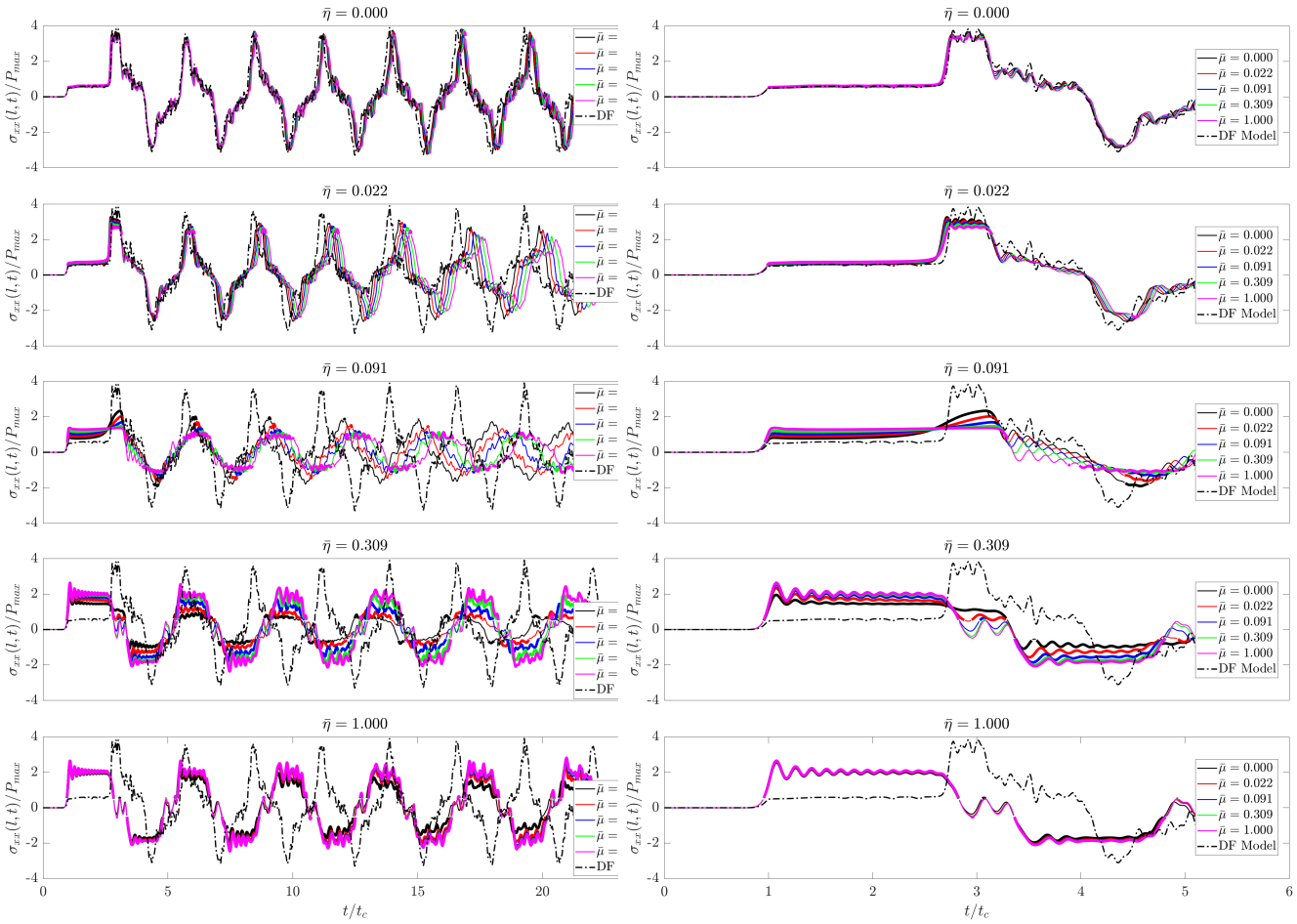

(a) (b)

Figure 18: History of the non-dimensional longitudinal stress at the distal end for Case 2 (Results grouped for $\bar{\mu}$ values): (a) response for the full duration; (b) zoomed the initial region.

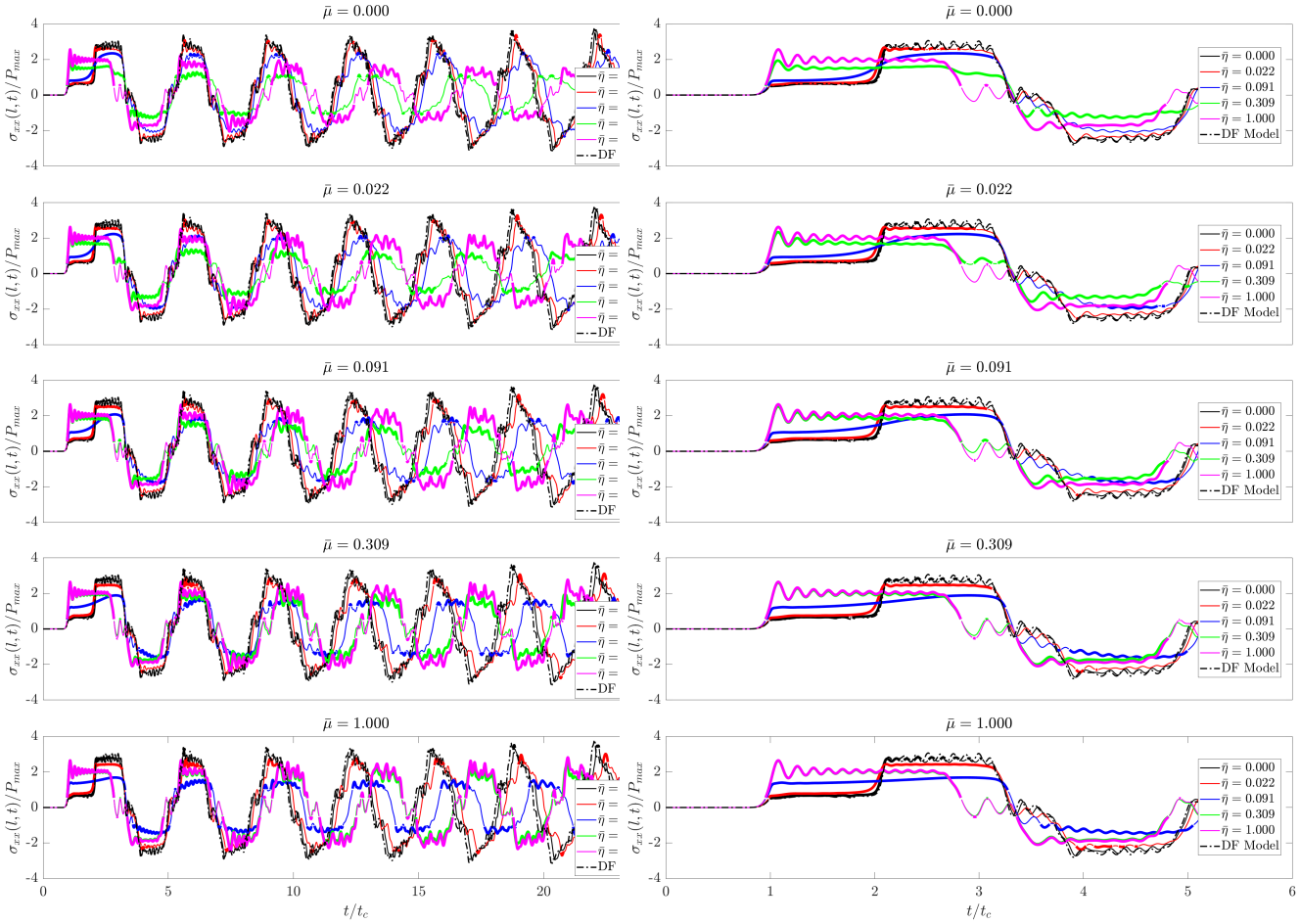

(a) (b)

Figure 19: History of the non-dimensional longitudinal stress at the distal end for Case 3 (Results grouped for $\bar{\eta}$ values): (a) response for the full duration; (b) zoomed the initial region.

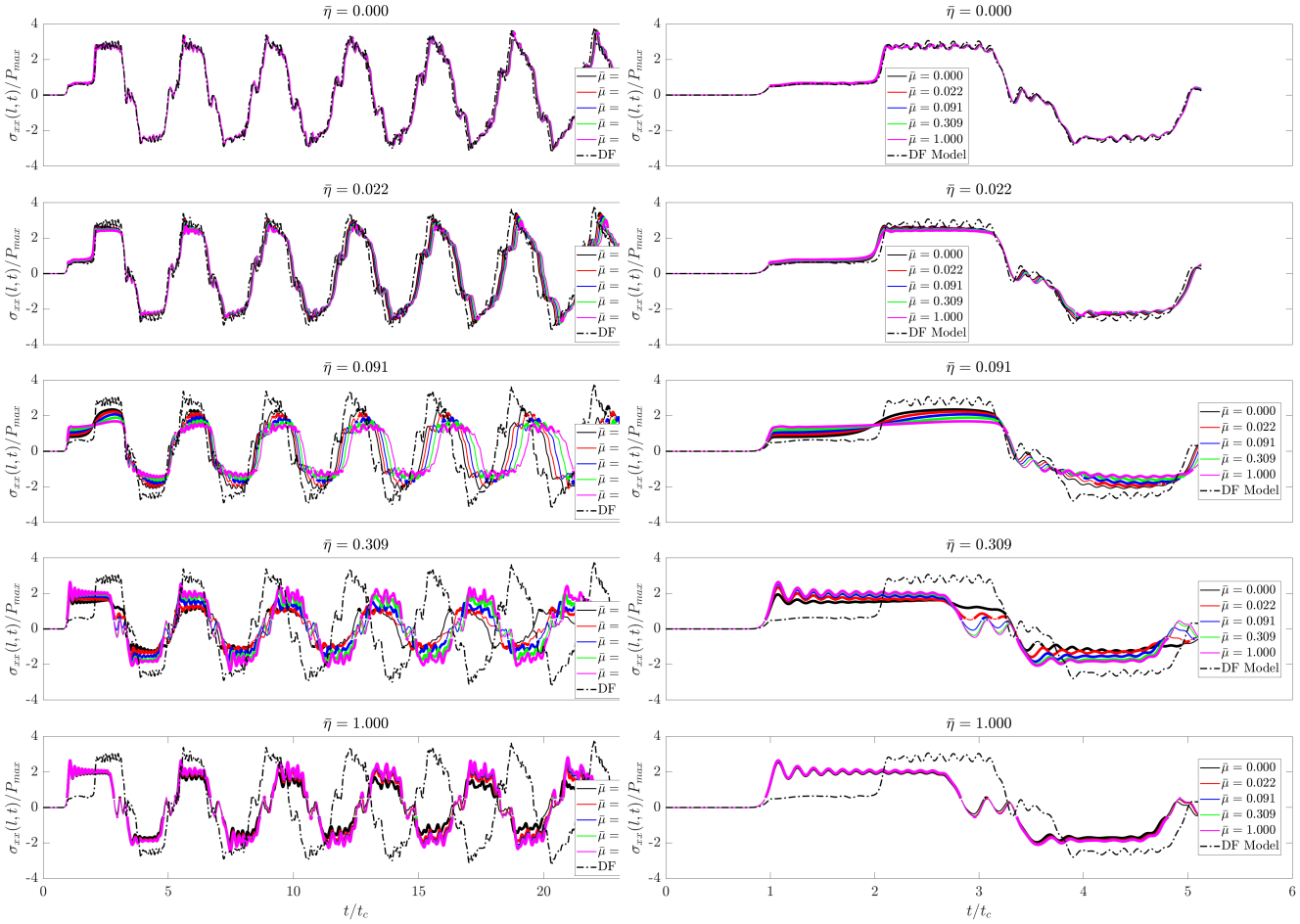

(a) (b)

Figure 20: History of the non-dimensional longitudinal stress at the distal end for Case 3 (Results grouped for $\bar{\mu}$ values): (a) response for the full duration; (b) zoomed the initial region.

A Numerical Implementation of the VP Model

For the numerical implementation of the VP model, we adopt a simplified return mapping algorithm, as explained below. The normal vector $\hat{\boldsymbol{n}}$ is split into $\hat{\boldsymbol{n}}_{\text{dev}}$ and $\hat{\boldsymbol{n}}_{\text{vol}}$ as

$$\hat{\boldsymbol{n}}_{\text{dev}} = \frac{3}{2\tilde{\sigma}}\boldsymbol{s}, \tag{15a}$$

$$\hat{\boldsymbol{n}}_{\text{vol}} = \frac{1}{3\tilde{\sigma}}\alpha^2\sigma_m\boldsymbol{I}, \tag{15b}$$

where,

$$\tilde{\sigma} = \sqrt{\frac{3}{2}\sigma_e^2 + \frac{\alpha^4}{3}\sigma_m^2} \tag{16}$$

Using (15) and (7), we get

$$\begin{aligned}\dot{\boldsymbol{\epsilon}}^p &= \dot{\boldsymbol{\epsilon}}^p_{dev} + \dot{\boldsymbol{\epsilon}}^p_{vol} \\ &= \dot{\gamma}\hat{\boldsymbol{n}}_{dev} + \dot{\gamma}\hat{\boldsymbol{n}}_{vol}\end{aligned} \tag{17}$$

A trite calculation yields the following expression for $\dot{\gamma}$:

$$\dot{\gamma} = \sqrt{\boldsymbol{\epsilon}^p_{dev} : \boldsymbol{\epsilon}^p_{dev} + 3{\boldsymbol{\epsilon}^p_{vol}}^2} \tag{18}$$

The computational algorithm employs a time discretization of the inelastic response. The viscoplastic state at time step $n+1$ is obtained from the known state at time step n and a specified incremental strain by means of a modified return mapping algorithm. Given $\boldsymbol{\epsilon}_n, \boldsymbol{\epsilon}^p_n, \boldsymbol{\sigma}_n, \hat{\epsilon}_n, \Delta\boldsymbol{\epsilon}$, we compute $\boldsymbol{\epsilon}^p_{n+1}, \boldsymbol{\sigma}_{n+1}, \hat{\epsilon}_{n+1}$ using the following predictor-corrector scheme.

Step-1: Elastic predictor

$$\begin{aligned}\boldsymbol{\epsilon}^{e,\text{tr}}_{n+1} &= \boldsymbol{\epsilon}^e_n + \Delta\boldsymbol{\epsilon} \\ \boldsymbol{\sigma}^{\text{tr}}_{n+1} &= \boldsymbol{\sigma}_n + \mathbf{D} : \boldsymbol{\Delta\epsilon}^{\mathbf{e,tr}}_{\mathbf{n+1}} \\ \bar{\epsilon}^{p,\text{tr}}_{n+1} &= \bar{\epsilon}^p_n \\ \sigma^{\text{tr}}_{y,n+1} &= \sigma_y(\bar{\epsilon}^p_n)\end{aligned} \tag{19}$$

Input : Trial stress $\boldsymbol{\sigma}^{\text{tr}}_{n+1}$, Trial yield stress $\sigma^{\text{tr}}_{y,n+1}$
Output: Updated variables $(\cdot)_{n+1}$
if $\phi(\boldsymbol{\sigma}^{tr}_{n+1}, \sigma^{tr}_{y,n+1}) \leq 0$ **then**
  $(\cdot)_{n+1} \leftarrow (\cdot)^{\text{tr}}_{n+1}$
  return
end
else
  Continue
end

Algorithm 1: Check for Viscoplastic Flow.

Step-3: Solve for $\Delta\gamma$ using Newton-Raphson method
The non-linear residual equation for $\Delta\gamma$ is given by:

$$\begin{aligned}R(\Delta\gamma) = \sigma_y\big|_{(\hat{\epsilon}+\Delta\gamma)}\Big(\mu\Delta\gamma + \Delta t\Big)^\eta \\ - \hat{\sigma}_{n+1}(\Delta t)^\eta\end{aligned} \tag{20}$$

The above equation is solved using the NR iterations using the derivative of $R(\Delta\gamma)$ wrt $\Delta\gamma$ as:

$$\begin{aligned} R(\Delta\gamma)' = \frac{\partial R(\Delta\gamma)}{\partial \Delta\gamma} &= \sigma_y\big|_{(\hat{\epsilon}+\Delta\gamma)} \mu\eta\Big(\mu\Delta\gamma + \Delta t\Big)^{\eta-1} \\ &+ H\big|_{(\hat{\epsilon}+\Delta\gamma)}\Big(\mu\Delta\gamma + \Delta t\Big)^{\eta} \\ &- \frac{d\hat{\sigma}_{n+1}}{d\Delta\gamma}(\Delta t)^{\eta} \end{aligned} \tag{21}$$

where,

$$\begin{aligned} \frac{d\hat{\sigma}_{n+1}}{d\Delta\gamma} &= \frac{\sigma_e^{\text{tr}}\sigma_{e,n+1}G' + \sigma_m^{\text{tr}}\sigma_{m,n+1}\lambda'}{(1+\alpha^2/9)\hat{\sigma}_{n+1}} \\ G' &= \left(\frac{-3G}{(1+\alpha^2/9)||\boldsymbol{n}^{\text{tr}}||\hat{\sigma}^{\text{tr}}}\right) \\ \lambda' &= \left(\frac{-\lambda\alpha^2}{3(1+\alpha^2/9)||\boldsymbol{n}^{\text{tr}}||\hat{\sigma}^{\text{tr}}}\right) \end{aligned} \tag{22}$$

Here, G is the shear modulus and λ is Lame's constant. Using Eq. (20) and Eq. (21), we use the standard NR approach to compute the updated value of $\Delta\gamma$ within each global time increment using the NR iterations, Eq. (23)).

$$\Delta\gamma_{k+1} = \Delta\gamma_k - \frac{R(\Delta\gamma)}{R'(\Delta\gamma)} \tag{23}$$

In the equation displayed above, k refers to the NR iteration step. The standard NR approach to compute the updated value of $\Delta\gamma$ within each global time increment, based on Eq. (20) is outlined in Algorithm 2.

Input : Initial guess $\Delta\gamma_n = \hat{\epsilon}_n$, Convergence tolerance tol_{NR}, Maximum NR iterations $\text{maxIter}_{\text{NR}}$,
Δt, μ, η, G, λ, α, $\boldsymbol{n}^{\text{tr}}$, $\hat{\epsilon}$, $\sigma_y(\cdot)$, $H(\cdot)$,
$\hat{\sigma}^{\text{tr}}_{n+1}$, σ^{tr}_e, σ^{tr}_m, $\hat{\sigma}^{\text{tr}}$
Output: Converged $\Delta\gamma_{n+1}$

Initialize $\Delta\gamma_k \leftarrow \hat{\epsilon}_n$
Initialize $k \leftarrow 0$
while $k < maxIter_{NR}$ **do**
  Compute $R(\Delta\gamma_k)$ `// Using Eq. (20)`
  Compute $R'(\Delta\gamma_k)$ `// Using Eq. (21)`
  $\Delta\gamma_{update} \leftarrow -R_{val}/R'_{val}$
  `// Update from Eq. (23)`
  $\Delta\gamma_{k+1} \leftarrow \Delta\gamma_k + \Delta\gamma_{update}$
  if $|R(\Delta\gamma_{k+1})| < tol_{NR}$ **then**
    return $\Delta\gamma_{k+1}$
    `// Converged within tolerance`
  end
  $\Delta\gamma_k \leftarrow \Delta\gamma_{k+1}$
  $k \leftarrow k + 1$
end
return *NR Failed to Converge*
`// Max iterations reached`

Algorithm 2: Newton-Raphson Iteration for $\Delta\gamma$.

Step-4: Update state variables

$$\boldsymbol{s}_{n+1} = \boldsymbol{s}^{\text{tr}}_{n+1}(1 - \Delta\gamma G') \tag{24a}$$

$$\sigma_{m,n+1} = \sigma^{\text{tr}}_{m,n+1}(1 - \Delta\gamma\lambda') \tag{24b}$$

$$\boldsymbol{\sigma}_{n+1} = \boldsymbol{s}_{n+1} + \sigma_{m,n+1}\boldsymbol{I} \tag{24c}$$

$$\hat{\epsilon}_{n+1} = \hat{\epsilon}_n + \Delta\gamma \tag{24d}$$

This completes the specification of the numerical algorithm that we implemented as a VUMAT in ABAQUS.

References

[1] AT Barnes et al. "Dynamic crushing of aluminum foams: Part I–Experiments". In: *International Journal of Solids and Structures* 51.9 (2014), pp. 1631–1645.

[2] Vikram S Deshpande and Norman A Fleck. "Isotropic constitutive models for metallic foams". In: *Journal of the Mechanics and Physics of Solids* 48.6-7 (2000), pp. 1253–1283.

[3] VS Deshpande and NA Fleck. "Multi-axial yield behaviour of polymer foams". In: *Acta materialia* 49.10 (2001), pp. 1859–1866.

[4] Chitralekha Dey et al. "Evaluation of optimum foam density for effective design of blast absorbers". In: *Mechanics of Advanced Materials and Structures* (2020), pp. 1–8.

[5] Chitralekha Dey et al. "Evaluation of optimum foam density for effective design of blast absorbers". In: *Mechanics of Advanced Materials and Structures* 29.3 (2022), pp. 400–407.

[6] Zhi Qiang Fan et al. “Stress Attenuation Mechanism of Foam Core Sandwich Panels Subjected to Close-Range Blast Loading”. In: *AMR* 945-949 (2014), pp. 561–566.

[7] S Gaitanaros and S Kyriakides. “Dynamic crushing of aluminum foams: Part II–Analysis”. In: *International Journal of Solids and Structures* 51.9 (2014), pp. 1646–1661.

[8] A. G. Hanssen, L. Enstock, and M. Langseth. “Close-range blast loading of aluminium foam panels”. In: *International Journal of Impact Engineering* 27.6 (2002), pp. 593–618.

[9] D Karagiozova, GS Langdon, and GN Nurick. “Blast attenuation in Cymat foam core sacrificial claddings”. In: *International Journal of Mechanical Sciences* 52.5 (2010), pp. 758–776.

[10] D Karagiozova, GS Langdon, and GN Nurick. “Propagation of compaction waves in metal foams exhibiting strain hardening”. In: *International Journal of Solids and Structures* 49.19-20 (2012), pp. 2763–2777.

[11] Tae-Rim Kim et al. “Constitutive modeling, computational implementation and material parameter identification for polymeric foams considering density and foaming direction”. In: *Mechanics of Materials* 162 (2021), p. 104029.

[12] Q.M. Li and H. Meng. “Attenuation or enhancement—a one-dimensional analysis on shock transmission in the solid phase of a cellular material”. In: *International Journal of Impact Engineering* 27.10 (2002), pp. 1049–1065.

[13] Tao Liu, HNG Wadley, and VS Deshpande. “Dynamic compression of foam supported plates impacted by high velocity soil”. In: *International Journal of Impact Engineering* 63 (2014), pp. 88–105.

[14] H. Ousji et al. “Air-blast response of sacrificial cladding using low density foams: Experimental and analytical approach”. In: *International Journal of Mechanical Sciences* 128-129 (2017), pp. 459–474.

[15] Djordje Perić. “On a class of constitutive equations in viscoplasticity: formulation and computational issues”. In: *International journal for numerical methods in engineering* 36.8 (1993), pp. 1365–1393.

[16] DD Radford et al. “The response of clamped sandwich plates with metallic foam cores to simulated blast loading”. In: *International Journal of solids and structures* 43.7-8 (2006), pp. 2243–2259.

[17] Andreas Schiffer et al. “Interaction of highly nonlinear solitary waves with rigid polyurethane foams”. In: *International Journal of Solids and Structures* 152 (2018), pp. 39–50.

[18] Michael W. Seitz and Beric W. Skews. “Effect of Compressible Foam Properties on Pressure Amplification During Shock Wave Impact”. In: *Shock Waves* 15.3-4 (2006), pp. 177–197.

[19] Juan C Simo and Thomas JR Hughes. *Computational inelasticity*. Vol. 7. Springer Science & Business Media, 2006.

[20] Eduardo A de Souza Neto, Djordje Peric, and David RJ Owen. *Computational methods for plasticity: theory and applications*. John Wiley & Sons, 2011.

[21] Puay Joo Tan et al. “Dynamic compressive strength properties of aluminium foams. Part I—experimental data and observations”. In: *Journal of the Mechanics and Physics of Solids* 53.10 (2005), pp. 2174–2205.

[22] Daniel Whisler and Hyonny Kim. “Experimental and simulated high strain dynamic loading of polyurethane foam”. In: *Polymer Testing* 41 (2015), pp. 219–230.

[23] Chenglin Yang and Stelios Kyriakides. "Continuum modeling of crushing of low density foams". In: *Journal of the Mechanics and Physics of Solids* 136 (2020), p. 103688.

[24] Ya Yang, Xiangzhen Kong, and Qin Fang. "Non-dimensional analysis on blast wave propagation in foam concrete: Minimum thickness to avoid stress enhancement". In: *Defence Technology* (2023).

[25] Ya Yang, Xiangzhen Kong, and Qin Fang. "Non-dimensional analysis on blast wave propagation in foam concrete: minimum thickness to avoid stress enhancement". In: *Defence Technology* 36 (2024), pp. 30–46.

[26] Jun Zhang et al. "Constitutive modeling of polymeric foam material subjected to dynamic crash loading". In: *International journal of impact engineering* 21.5 (1998), pp. 369–386.